THz detection of small molecule vapors in the atmospheric transmission windows

Joseph S. Melinger,[1,*] Yihong Yang,[2] Mahboubeh Mandehgar,[2] and D. Grischkowsky[2]

[1] *Electronics Science and Technology Division, Naval Research Laboratory, Washington, DC 20375 USA*
[2] *School of Electrical and Computer Engineering, Oklahoma State University, Stillwater, OK 74078 USA*
[*] *joseph.melinger@nrl.navy.mil*

Abstract: Using a low power beam of ultrashort THz pulses that propagate in the ambient laboratory environment we have measured the rotational signatures of small molecule vapors at frequencies within the atmospheric transmission windows. We investigate two types of apparatus. In the first type the THz beam propagates along a 6.7 meter round trip path that is external to the spectrometer, and which contains a long sample tube (5.4 meter round trip path) that holds the analyte vapor. The environment of the tube is controlled to simulate dry or humid conditions. In the second apparatus the THz beam propagates over a much longer 170 meter round trip path with analyte vapor contained in a relatively short 1.2 meter round trip path sample chamber. We describe the rotational signatures for each apparatus in the presence of the strong interference from water vapor absorption. For the shorter path long-tube apparatus we find that the peak detection sensitivity is sufficient to resolve a 1% absorption feature. For the more challenging 170 meter path apparatus we find that the peak detection sensitivity is sufficient to resolve a 3-5% absorption feature. The experiments presented here represent a first step towards using ultrashort THz pulses for coherent broad band detection of small molecule gases and vapors under ambient conditions.

OCIS codes: (300.6495) Terahertz spectroscopy; (010.1320) Atmospheric transmission.

References and links

1. D. E. Burch and D. A. Gryvnak, "Continuum absorption by water vapor in the infrared and millimeter regions," *in Atmospheric Water Vapor*, A. Deepak, T.D. Wilkerson, and L.H. Ruhnke, eds. (Academic Press, 1980).
2. Yu. A. Dryagin, A. G. Kislyakov, L. M. Kukin, A. I. Naumov, and L. I. Fedosyev, "Measurement of atmospheric absorption of radio waves in the range 1.36-3.0 mm," Isvestya VUZ Radiosphsica **9**, 624–627 (1966).
3. V. Ya. Ryadov and N. I. Furashov, "Investigation of the spectrum of radiowave absorption by atmospheric water vapor in the 1.15 to 1.5 mm range," Radio Phys. Quantum Electron. **15**(10), 1124–1128 (1972).
4. D. E. Burch, "Absorption of Infrared Radiant Energy by CO_2 and H_2O. III. Absorption by H_2O between 0.5 and 36 cm^{-1}," J. Opt. Soc. Am. **58**(10), 1383–1394 (1968).
5. T. Kuhn, A. Bauer, M. Godon, S. Bühler, and K. Künzi, "Water vapor continuum: absorption measurements at 350 GHz and model calculations," J. Quant. Spectrosc. Radiat. Transf. **74**(5), 545–562 (2002).
6. R. E. Hills, A. S. Webster, D. A. Alston, P. L. R. Mores, C. C. Zammit, D. H. Martin, D. P. Rice, and E. I. Robson, "Absolute measurements of atmospheric emission and absorption in the range 100-1000 GHz," Infrared Phys. **18**(5-6), 819–825 (1978).
7. V. B. Podobedov, D. F. Plusquellic, and G. T. Fraser, "Investigation of the water-vapor continuum in the THz region using a multipass cell," J. Quant. Spectrosc. Radiat. Transf. **91**(3), 287–295 (2005).
8. V. B. Podobedov, D. F. Plusquellic, K. E. Siegrist, G. T. Praser, Q. Ma, and R. H. Tipping, "New measurements of the water vapor continuum in the region from 0.3 to 2.7 THz," J. Quant. Spectrosc. Radiat. Transf. **109**(3), 458–467 (2008).
9. E. Serabyn and E. W. Weisstein, "Calibration of planetary brightness temperature spectra at near-millimeter and submillimeter wavelengths with a Fourier-transform spectrometer," Appl. Opt. **35**(16), 2752–2763 (1996).
10. J. R. Pardo, E. Serabyn, and J. Cernicharo, "Submillimeter atmospheric transmission measurements on Mauna Kea during extremely dry El Nino Conditions: implications for broadband opacity contributions," J. Quant. Spectrosc. Radiat. Transf. **68**(4), 419–433 (2001).
11. A. I. Meshkov and F. C. De Lucia, "Laboratory measurements of dry air atmospheric absorption with a millimeter wave cavity ring down spectrometer," J. Quant. Spectrosc. Radiat. Transf. **108**(2), 256–276 (2007).

#160928 - $15.00 USD Received 4 Jan 2012; revised 20 Feb 2012; accepted 21 Feb 2012; published 8 Mar 2012

12. H. J. Liebe, “The atmospheric water vapor continuum below 300 GHz,” Int. J. Infrared Millim. Waves **5**(2), 207–227 (1984).
13. H. J. Liebe, “MPM-an atmospheric millimeter-wave propagation model,” Int. J. Infrared Millim. Waves **10**(6), 631–650 (1989).
14. J. R. Pardo, J. Cernicharo, and E. Serabyn, “Atmospheric transmission at microwaves (ATM): An improved model for millimeter/submillimeter applications,” IEEE Trans. Antenn. Propag. **49**(12), 1683–1694 (2001).
15. F. C. De Lucia, “Spectroscopy in the THz spectral region,” in *Sensing with THz Radiation*, D. Mittleman ed. (Springer-Verlag, 2003).
16. N. Gopalsami and A. C. Raptis, “Millimeter-wave radar sensing of airborne chemicals,” IEEE Trans. Microw. Theory Tech. **49**(4), 646–653 (2001).
17. H. B. Liu, H. Zhong, N. Karpowicz, Y. Chen, and X.-C. Zhang, “Terahertz Spectroscopy and Imaging for Defense and Security Applications,” Proc. IEEE **95**(8), 1514–1527 (2007).
18. Y. Yang, A. Shutler, and D. Grischkowsky, “Measurement of the transmission of the atmosphere from 0.2 to 2 THz,” Opt. Express **19**(9), 8830–8838 (2011).
19. Y. Yang, M. Mandeghar, and D. Grischkowsky, “Broad-band THz pulse transmission through the atmosphere,” IEEE Trans. Terahertz Sci. Technol. **1**(1), 264–273 (2011).
20. J. S. Melinger, A. Shutler, Y. Yang, and D. Grischkowsky, “Long path THz detection of small molecule vapors in the atmospheric transparency windows.” Conference on Lasers and Electro-Optics CLEO-2011 OSA Technical Digest (Optical Society of America, Washington, D.C., 2011), CThEE7.
21. R. A. Cheville and D. Grischkowsky, “Foreign and self broadened rotational linewidths of high temperature water,” J. Opt. Soc. Am. B **16**(2), 317–322 (1999).
22. M. Kessler, H. Ring, R. Tramborulo, and W. Gordy, “Microwave spectra and molecular structure of methyl cyanide and isomethyl cyanide,” Phys. Rev. **79**(1), 54–56 (1950).
23. R. Bocquet, G. Wlodarczak, A. Bauer, and J. Demaison, “The sub-millimeter wave rotational spectrum of methyl cyanide: Analysis of the ground and low-lying excited vibrational states,” J. Mol. Spectrosc. **127**(2), 382–389 (1988).
24. H. Harde, S. Keiding, and D. Grischkowsky, “THz commensurate echoes: Periodic rephasing of molecular transitions in free-induction decay,” Phys. Rev. Lett. **66**(14), 1834–1837 (1991).
25. D. Mittleman, R. H. Jacobsen, R. Neelamani, R. G. Baraniuk, and M. C. Nuss, “Gas sensing using terahertz time domain spectroscopy,” Appl. Phys. B **67**(3), 379–390 (1998).
26. H. M. Pickett, R. L. Poynter, E. A. Cohen, M. L. Delitsky, J. C. Pearson, and H. S. P. Muller, “Sub-millimeter, millimeter, and microwave spectral line catalog,” J. Quant. Spectrosc. Radiat. Transf. **60**(5), 883–890 (1998). Access to specific catalog entries may be found at http://spec.jpl.nasa.gov/
27. L. S. Rothman, E. Gordon, A. Barbe, D. Chris Brenner, P. F. Bernath, M. Birk, V. Boudon, L. R. Brown, A. Campargue, J. P. Champion, K. Chance, L. H. Coudert, V. Dana, V. M. Devi, S. Fally, J. M. Flaud, R. R. Gamache, A. Goldman, D. Jacquemart, I. Kleiner, N. Lacome, W. J. Lafferty, J. Y. Mandin, S. T. Massie, S. N. Mikhailenko, C. E. Miller, N. Moazzen-Ahmadi, O. V. Naumenko, A. V. Nikitin, J. Orphal, V. I. Perevalov, A. Perrin, A. Predoi-Cross, C. P. Rinsland, M. Rotger, M. Simeckova, M. A. H. Smith, K. Sung, S. A. Tashkun, J. Tennyson, R. A. Toth, A. C. Vandaele, and J. Vander Auwera, “The HITRAN 2008 molecular spectroscopic database,” J. Quant. Spectrosc. Radiat. Transf. **110**(9-10), 533–572 (2009).
28. T. Hattori, K. Egawa, S. Ookuma, and T. Itanani, “Intense terahertz pulses from large aperture antenna with interdigitated electrodes,” Jpn. J. Appl. Phys. **45**(15), L422–L424 (2006).
29. F. C. De Lucia, D. A. Petkie, and H. O. Everitt, “A double resonance approach to submillimeter terahertz remote sensing at atmospheric pressure,” IEEE J. Quantum Electron. **45**(2), 163–170 (2009).
30. C. D. Boone, K. A. Walker, and P. F. Bernath, “An efficient analytical approach for calculating line mixing in atmospheric remote sensing applications,” J. Quant. Spectrosc. Radiat. Transf. **112**(6), 980–989 (2011).
31. M. van Exter and D. Grischkowsky, “Characterization of an optoelectronic teraHz beam system,” IEEE Trans. Microw. Theory Tech. **38**(11), 1684–1691 (1990).
32. C. Johnson, F. J. Low, and A. W. Davidson, “Germanium and germanium-diamond bolometers operated at 4.2 K, 2.0K, 1.2K, 0.3K, and 0.1K,” Opt. Eng. **19**, 255 (1980).
33. D. Grischkowsky, S. Keiding, M. van Exter, and C. Fattinger, “Far-infrared time-domain spectroscopy with TeraHz beams of dielectrics and semiconductors,” J. Opt. Soc. Am. B **7**, 2006–2015 (1990).
34. P. R. Griffiths and J. A. de Haseth, *Fourier Transform Infrared Spectrometry* (John Wiley, New York, 1986), Chaps. 2 and 7.

---

1. Introduction

The remote sensing of molecular gases and vapors in the region between 0.1 – 1.0 THz is a challenging problem, in part because of strong absorption of THz radiation by atmospheric water vapor. Even so, there are windows of relatively high transmission, especially at the lower THz frequencies, where transmission over paths greater than 100 meters is feasible. The historic Fig. 1 given below shows experimental measurements and a theoretical prediction of THz power attenuation due to atmospheric water vapor from 0.1 to 1.0 THz [1]. The predicted THz attenuation (dB/km) given by curve A in Fig. 1 is based on the sum of the calculated attenuation of all the water vapor lines, plus (curve B) an additional “extra water vapor absorption”, which is needed to explain the experimental data. While the THz attenuation

#160928 - $15.00 USD Received 4 Jan 2012; revised 20 Feb 2012; accepted 21 Feb 2012; published 8 Mar 2012

changes by nearly five orders of magnitude over this region, significant THz propagation can occur in the relatively transparent regions (indicated by the blue lines). At a water vapor density of 5.9 g/m^3 (relative humidity of about 34% at 20 °C) the predicted THz propagation length with 10 dB of loss is about 2 kilometers at 0.3 THz and about 125 meters at 0.93 THz. These propagation lengths are potentially useful for gas and vapor sensing applications.

In the lower frequency range from 0.1 – 0.3 THz there have been several examples of long path THz propagation in the context of measuring attenuation due to water vapor absorption. Using backward wave oscillator (BWO) sources field measurements of atmospheric THz attenuation were performed by Dryagin et al. [2] and Ryadov et al. [3]. In the case of Ref [3], output power as high as 300 mW was used. These studies achieved propagation paths of several kilometers, depending on the frequency used. At higher frequencies up to 1.1 THz, long path THz measurements have been made in the controlled laboratory environment. An example is that of Burch who used multi-pass Fourier transform spectroscopy in a sample chamber to propagate THz radiation over paths as long as 469 meters and thereby measure THz attenuation due to water vapor in the region between 0.15 – 1.1 THz [4].

More recently, the far-infrared studies of water vapor in the atmosphere have concentrated on determining and understanding the water vapor continuum absorption with respect to its importance to ground-based astronomy, remote sensing, and satellite-based applications [5–10]. These studies include measurements using single frequency sources [5] and broadband Fourier transform spectrometers (FTS) [6–10]. Some of this work has described laboratory measurements over a large range of water vapor pressure and temperature [5,7,8], and some has been conducted at ground-based astronomy sites [6,9,10], including the presentation of the zenith transmission spectrum of the atmosphere from 350 GHz to 1050 GHz at Mauna Kea during the extremely dry El Nino conditions [10]. These works [6–10] were based on far-infrared FTS measurements, which will be described and compared to the THz time-domain spectroscopy (THz-TDS) measurements presented in this paper (see the Appendix). Absorption due to the dry air continuum is also of considerable importance for atmospheric propagation. Recently, laboratory measurements of the dry air continuum have been reported using the cavity ring down method [11]. An important goal of the measurements in references [1–11] is towards developing and refining theoretical models that predict atmospheric transmission in the millimeter-wave and submillimeter/THz regions [12–14]. Finally, numerous atmospheric studies have been made at high altitudes using aircraft and balloon platforms. A description of some of these works may be found in reference [15].

For active detection of analyte vapors at ground level, cw techniques have been applied in the window from 0.22 – 0.30 THz to the field detection of gases. Gopalsami et al. developed a millimeter radar chemical sensor based on a BWO source [16]. Using rapid scanning of the BWO they attempted field detection of a methylchloride plume at a distance of 60 meters from the source. The tunability of the BWO was sufficient to overlap three of the methylchloride pressure broadened rotational bands.

In contrast, there have been relatively few studies of broadband coherent THz pulse propagation in the atmosphere. In one example Liu et al. demonstrated ultrashort THz pulse propagation over a 100 meter path at 10% relative humidity [17]. Here, most of the observed low frequency attenuation was due to frequency dependent power transfer losses in the THz propagation system. More recently, Yang et al. have used THz-TDS with optoelectronic antennas to characterize THz attenuation due to water vapor from 0.2 – 2 THz over a 6.2 meter path [18]. However, THz detection of analyte vapors in the ambient atmosphere using broadband ultrashort THz pulses has not been previously demonstrated.

An important motivation for using a coherent broadband THz-TDS system is the potential to transmit significant spectral amplitude over relatively long paths in each of the atmospheric transparency windows. For small molecule gases and vapors that have sufficiently resolved rotational structure at atmospheric pressure, broadband detection provides an opportunity to simultaneously detect a relatively large number of rotational lines (or bands) in the transparency windows, which can increase the robustness of identification. Recently, Yang et al. described a long-path apparatus that transmitted ultrashort THz pulses through the atmosphere over a path of 167 meters with efficient coupling to the receiver for frequencies between 0.1 and 1.6 THz [19]. Even with significant losses due to water vapor absorption, diffraction, and coupling back to the receiver the returned THz pulse could be detected with high signal to noise (~200:1). This demonstration leads to the opportunity to investigate the use of long-path THz-TDS to remotely detect gases and vapors. In this paper we describe experiments that detect the rotational spectra of small molecule vapors under conditions of ambient pressure and temperature, and where the THz beam propagates over relatively long path lengths that are external to the conventional short THz beam path (~50 cm) within the spectrometer. We compare two cases. First, where the THz beam propagates over a round trip external path of 6.7 meters in an environmentally controlled long-tube chamber [20], and second, where the THz beam propagates over a much longer 170 meter open path in the ambient laboratory environment. We describe the relevant observables for long path THz-TDS detection of the rotational signatures in both the time and frequency domains. We also discuss the detection sensitivity achievable with the current apparatus and the types of molecular vapors for which specificity is achievable under ambient conditions.

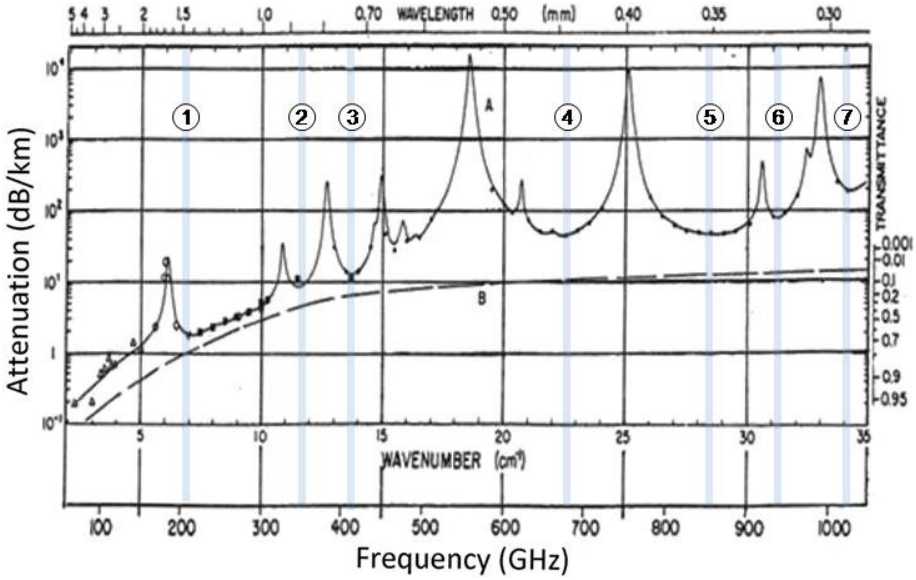

Fig. 1. This figure is a revised version of Fig. 10 of [1] with the caption, "Spectral plots of the near-millimeter attenuation by the atmospheric H_2O at sea level. H_2O density = 5.9 g/m^3. Curve A represents attenuation calculated by summing the theoretical contributions by all the lines and adding the continuum represented by curve B. The H_2O density corresponds to a relative humidity of 34% at 20 °C. The symbols represent experimental measurements of several groups which are referenced in Ref [1]. The blue lines with circled numbers indicate the regions of relative transparency that overlap with the THz-TDS bandwidth.

2. Experimental

Two experimental apparatus are used for measurement of analyte vapors contained within a path external to a conventional THz spectrometer. The first apparatus transmits the THz beam over a roundtrip path length of 6.7 meters. The beam path includes propagation in a long tube chamber where analyte vapors can be introduced. This apparatus will be referred to as the "long-tube" apparatus. The second apparatus transmits the THz beam over a much longer path of 170 meters and is called a "long-path" apparatus. Both of these apparatus are based on a modified optoelectronic THz-TDS spectrometer and were initially described in references [18] and [19]. We briefly describe these apparatus below with some modifications for the detection of vapors.

2.1 Long-tube apparatus

A schematic of the long-tube apparatus is shown in Fig. 2. The THz spectrometer is contained in dry-air purged box #1. The THz beam is coupled out of the spectrometer by a removable mirror pair and into dry-air purged box #2 through a 15 cm diameter thin (12.5 µm) film plastic window, which is highly transparent and has very little reflection. Box #2 is connected to a 6” (15.24 cm) inner diameter commercial PVC pipe. Both ends of the pipe are sealed with thin film plastic windows so that it encloses an air-tight round trip path length of 5.4 meters. The THz beam is returned through the tube and to the receiver using a 6” (15.24 cm) diameter concave spherical mirror with a 120” (3.04 m) radius of curvature. The total extra round trip distance of the path external to the standard spectrometer path is 6.7 meters. This distance is equal to 2 round trips of the ultrafast pulses in the titanium sapphire pump laser cavity with a repetition rate of 89.695 MHz. Therefore, to gate the receiver we use the second pulse down the pulse train from the optical pulse that gates the transmitter (see Fig. 2).

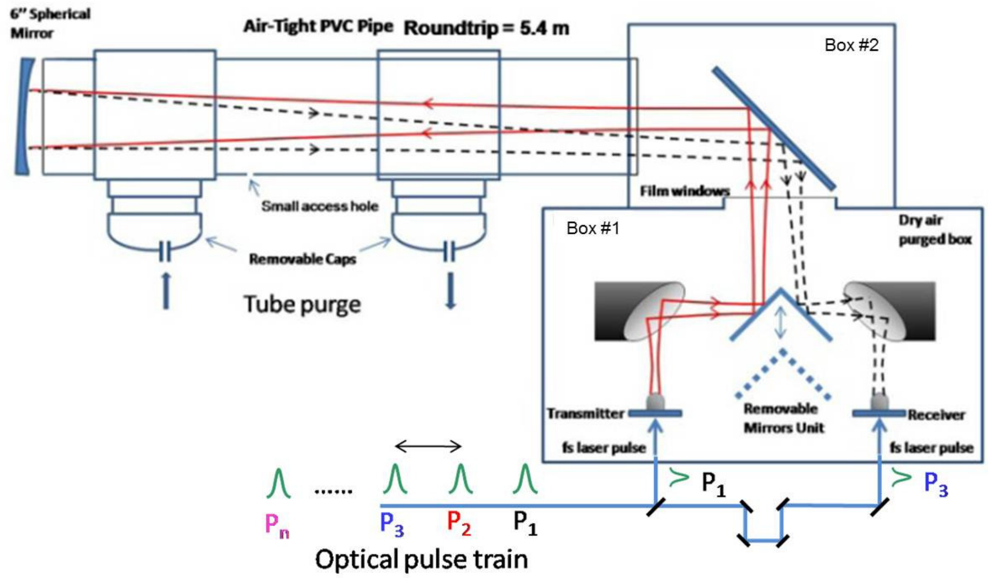

Fig. 2. Long-tube apparatus based on a standard THz-TDS spectrometer. A pair of removable mirrors deflects the THz beam out of the spectrometer and into Box #2. The beam then enters a 5.4 meter round trip path length enclosed tube for vapor measurements. The THz pulse returned to the receiver is gated by the 2nd pulse (P3) down train from the pulse that excites the transmitter (P1).

The PVC tube contains two ports so that the tube can be purged with dry air or ambient air. The tube also contains a small hole (diameter < 1 mm) in the side where vapor can be introduced with a syringe, or from drops of a volatile liquid. The measurement sequence is as follows. For measurements in a relatively dry environment the tube is first purged with dry air to a reach a desired relative humidity. Then the tube is sealed for subsequent THz waveform measurements. For measurements at ambient humidity, laboratory air is first circulated through the tube for several minutes. Reference scans are measured over a scan length of 166 ps corresponding to a spacing between points in the frequency domain of 6.1 GHz. The sample vapor is then introduced and signal scans are measured over the same time base. The lock-in amplifier time constant is set to 30 ms and a waiting time of 120 ms is used. A 40 micron step size is used for the waveform scan leading to 625 data points (0.26667 ps/step). In the current apparatus a single scan takes approximately 180 seconds to complete. Based on these lockin amplifier settings an optimized system might in principle approach only 75 seconds to complete a single scan. Typically, four reference and signal waveforms are averaged. The averages are then zero-padded to 1650 ps and Fourier transformed to obtain spectral amplitudes. The zero-padding performs an interpolation in the frequency domain but does not improve the spectral resolution. The measured spectral amplitude is broadened by the convolution with the instrument spectral window [21]. The window can be modeled as a sinc function $\sin(2\pi\nu T)/(2\pi\nu T)$, with FWHM = 0.609/T, where T is the effective time window. Therefore, for the 166 ps time window, the experimental frequency response is convoluted with the 3.67 GHz FWHM spectral window function.

2.2 Long-path apparatus

A schematic of the long-path apparatus is shown below in Fig. 3. The current 170 meter path apparatus is based on the original 10 mirror 167 meter path design [19], but lengthened slightly by 3 meters. The apparatus uses the same THz-TDS spectrometer but differs from the long-tube apparatus in several ways. First, the entire apparatus (with the exception of the sample tube) including the spectrometer is in the ambient environment. Second, to reduce diffraction losses relatively large mirrors (Edmund Optics) are used to guide the THz beam. The collimating mirror M3 has a diameter of 12.5" (32 cm) and a 125" (317.5 cm) focal length. M4 = 16" x 24", M5 = 12" x 12", and M6-M10 = 16" x 24". Third, the sample tube consists of a 12" (30.5 cm) diameter 24" (61 cm) long clear Plexiglas tube fitted with air-tight thin film plastic windows on both ends. For convenience the sample tube is placed on the optical table between mirrors M2 and M3 (In principle, placement anywhere along the path would effectively result in the same double pass). The total round trip sample path length is 1.2 meters, which is 4.5 times shorter than the long tube described above. The gating of the returned THz pulse is accomplished using the 52nd laser pulse down the optical train from the laser pulse that excites the transmitter.

The alignment of the THz beam is quite stable considering that it first propagates along an optical table via M1-M4, and then propagates through the rest of the laboratory using floor-mounted mirrors (M5-M9). There is a slow thermal drift in the pulse train of about 0.6 ps/hr, corresponding to a drift of 180 μm/hr, which is about 1 part-per-million of the 170 meter path. The thermal drift is quite slow compared to the three minute measurement time to scan a waveform.

The repetition rate of the mode-locked laser without any special features is quite stable at 89.6948(x)(x) MHz with frequency drift and some jitter in the last 2 digits indicated by x in the open brackets. The above repetition frequency corresponds to a delay between pulses of 11.148918 ns, which is multiplied by 51 to give the total laser-clock defined long-path delay of 568.594835 ns. Over the course of an experiment, there are slow changes of the order of 100 Hz. If the clock rate is reduced to 89.6947 MHz, the corresponding total time delay is increased to 568.595469 ns, causing a difference in the total long-path clock delay of 0.63 ps. This change in delay is easily measured and is almost equal to our observed drift of 0.6 ps/hour [19].

Our total drift is caused by both the laser-clock drift, which is easily measured by the frequency counter and by the slow drift of the length of the 170 m long THz optical train. A 149 m-long part of the 170 m optical train is directed by heavy optical mirror mounts supported by the thick floating concrete slab floor of the basement laboratory. The other 21 m-long part of the THz optical train is on the stainless steel (s.s.) optical table. The massive floor is considered to respond very slowly, on the order of many hours or days, to average temperature changes, while the temperature response of s.s. table is much faster. It is important to note that for both stainless steel and concrete, the coefficient of thermal expansion is approximately $(\Delta L/L) = 10^{-5}/\ ^\circ C$. Consequently, if the temperature difference ΔT between the concrete floor and the s.s. optical table remained the same, the measured start time of the long-path transmitted THz pulse would not change. However, if the difference temperature ΔT changed by 1 °C, a length difference of 170 m x 10^{-5}would occur, with the corresponding change in the start time of the THz pulse of 5.7 ps. This time change is quite significant and is easily observed.

#160928 - $15.00 USD Received 4 Jan 2012; revised 20 Feb 2012; accepted 21 Feb 2012; published 8 Mar 2012

In general, for measurements in the time domain, changes in the starting time of the measured signal cause frequency-dependent phase changes in the corresponding complex spectra. However, if there is no significant time drift during the time duration of the measurement, the amplitude spectra of the corresponding signals do not change. Consequently, under such conditions, averaging of many pulses should involve averaging of their amplitude spectra.

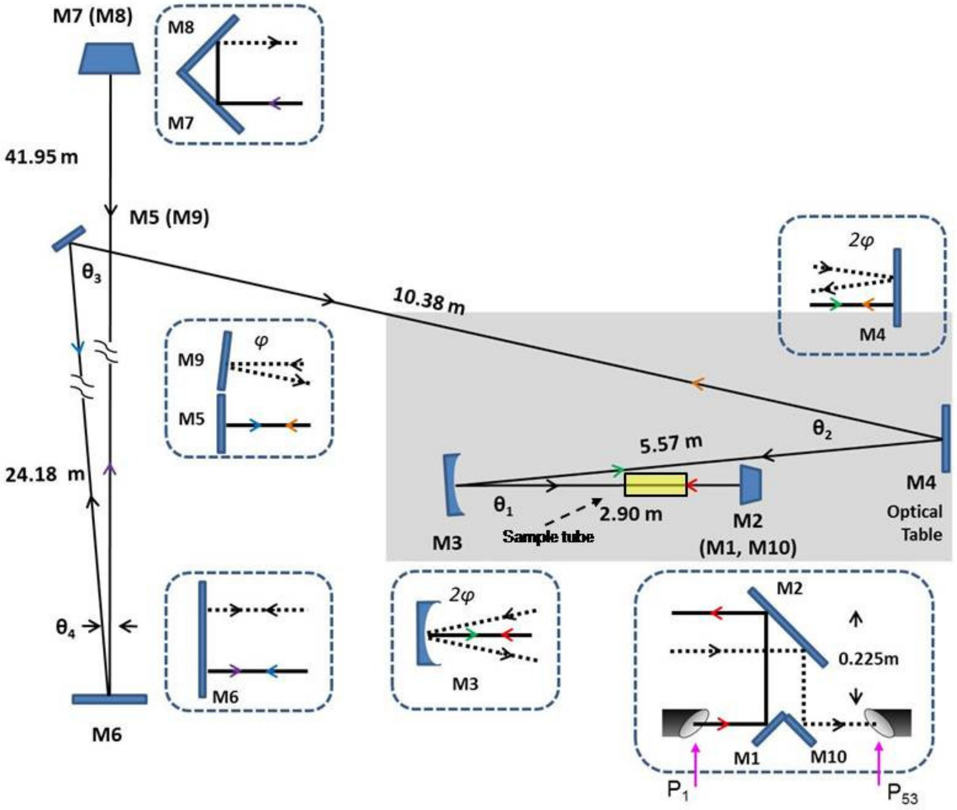

Fig. 3. Schematic from the top (x-z plane) of the 170 meter round trip long path apparatus consisting of 10 mirrors. Insets: Side view (y-z plane) of the mirrors. The solid lines show the path of the THz beam deflected out of and into the spectrometer by the mirror pair M1 and M10. The position of the THz-TDS spectrometer is shown in the inset and lies underneath M2. The THz pulse returned to the receiver is gated by the 52nd pulse down the laser pulse train from the excitation pulse. The indicated angles are $\theta_1 = 5.4°$, $\theta_2 = 19°$, $\theta_3 = 77°$, $\theta_4 = 2.4°$, and $\phi = 1.25°$.

The alignment of the long-path THz optical train is surprisingly stable, requiring no adjustments over periods as long as two-weeks. The main stability issue involves the reproducibility of the THz input pulses to the optical train, caused by changes in the laser driving and sampling pulses and their incoming beam directions, and their precise focusing on the transmitter and receiver antennas. This problem is best characterized by measuring several input THz pulses and comparing the ratio R(ω) of their individual amplitude spectra to their average. For high-sensitivity operating conditions R(ω) = 1.00 ± 0.005; for acceptable operating conditions R(ω) = 1.00 ± 0.01. If these ratios cannot be achieved, then the laser alignment and laser beam alignment and focusing on the THz transmitter and receiver antennas are adjusted for optimum response and stability. Typically, we have several days of operation until such adjustments, which are usually relatively minor, are needed.

The data acquisition parameters used in the long-tube measurements is also used in the long-path measurements. The following sequence is used to perform long-path measurements of analyte vapors contained in the sample tube. First, the system operation and stability are checked by measuring the performance of the THz-TDS system with the coupling mirrors removed. This measurement gives the input pulse to M1. Second, the coupling mirrors (M1 and M10) are installed with no mirror alignment necessary. The THz pulse train then propagates through the 170 meter path making a double pass through the sample cell containing only ambient laboratory air. The pulse train returned to the receiver is measured and this waveform serves as the reference. After measurement of typically six to eight reference waveforms the sample tube is loaded with an analyte vapor through a small hole in the side of the tube. The signal waveform is then measured and repeated six to eight times. Each reference and signal waveform is zero padded to 1650 ps and then Fourier transformed to give spectral amplitudes. From these measurements the average signal and reference spectral amplitudes are calculated. We found that the S/N improved with the square root of the number of spectral amplitudes averaged up to nine. Further averaging requires too much time, and system drift can become an issue.

3. Results and discussion

3.1 Effect of the external path propagation on the THz pulse and spectrum

To begin we compare the THz pulse and spectrum before and after the external path propagation. Figure 4 below shows experimental waveforms and spectral amplitudes of the input THz pulse to M1, the THz pulse returned after propagating through the long-tube apparatus (total round trip path 6.7 meter) at 51% relative humidity (RH), and the THz pulse returned after the 170 meter round trip propagation through the long path apparatus at 50% RH. The “input” THz pulse (bottom black curve) is the pulse that propagates in the nearly dry 50 cm path spectrometer and is a clean nearly single cycle pulse with a spectral amplitude containing frequency components to about 2 THz. The small dips in the spectral amplitude are due to residual water vapor in the dry box with humidity less than RH 0.5%. A single waveform is measured with a peak signal to noise ratio (S/N) of about 5000:1. The average input power was 30 nW. The THz pulse after propagating through the long-tube apparatus is shown (multiplied by 4) as the middle red curve. The peak amplitude has been reduced due to input and output coupling and water vapor absorption. The strong oscillations are due to the interaction with water vapor at 51% RH. The waveform in this case is detected with a peak S/N of approximately 500:1. The strong water vapor rotational transitions shown in the amplitude spectrum (middle red curve) result in essentially complete absorption of the spectral amplitude about the center frequencies. Weaker water vapor lines are easily observed at 0.380 THz, 0.443 THz, and 0.620 THz. We also note the appearance of some broad modulations on the spectral amplitude. The most notable are centered at 0.2 THz and 0.25 THz, but they also appear elsewhere. These modulations are not due to water vapor, rather they are likely due to slight clipping of the THz beam on the inner surface as the beam propagates through the long tube. The same modulations are present in both the reference and signal and therefore can be largely cancelled out in the absorbance spectra. Despite the strong effect of water vapor the spectral amplitude retains broad transmission windows to about 1.6 THz which can be used for detection of rotational resonances of analyte vapors.

#160928 - $15.00 USD Received 4 Jan 2012; revised 20 Feb 2012; accepted 21 Feb 2012; published 8 Mar 2012

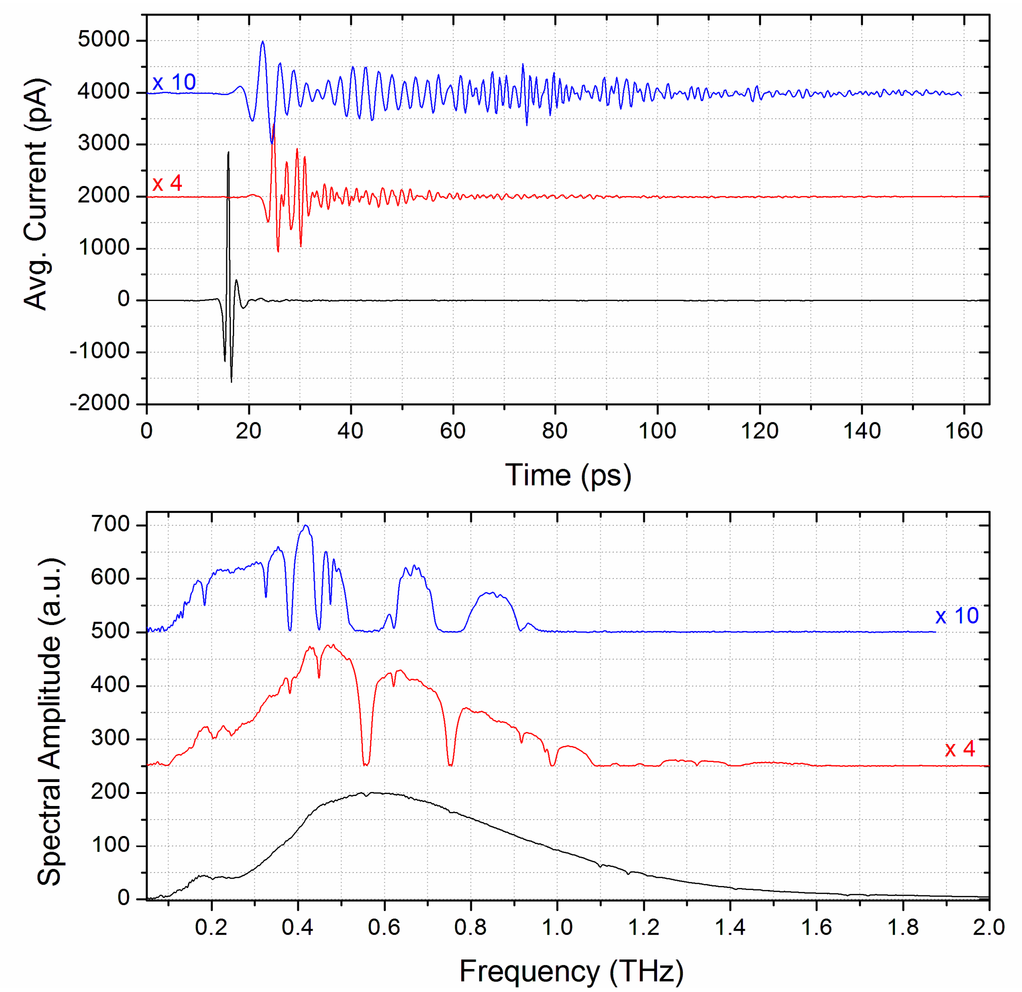

Fig. 4. Experimental waveforms (top) and spectral amplitudes (bottom). The input THz pulse to M1 and spectrum are indicated by the bottom black curves. The weak strength of the observed water lines indicates that the humidity was less than 0.5% RH in the dry-air purged Box No. 1. The THz pulse/spectrum returned to the receiver after propagating over the 6.7 meter path at 51% RH in the long-tube apparatus are indicated by the middle red curves and multiplied by a factor of 4. The THz pulse/spectrum after the 170 meter propagation at 50% RH in the long-path apparatus are shown by the top blue curves and multiplied by a factor of 10. For clarity, the red and blue curves are offset.

The THz pulse and spectral amplitude after propagating 170 meters at 50% RH in the long-path apparatus are shown above as the top blue curves in Fig. 4. Here, the interaction with the water vapor rotational transitions has dramatically broadened the oscillatory pattern so that the oscillatory signatures are still visible at 160 ps. The broadening of the oscillatory pattern has been attributed in part to group velocity dispersion resulting in a frequency swept waveform, with the higher frequency components trailing the lower frequency components [19]. The peak amplitude has been further reduced by the increased water vapor absorption and losses due to the frequency dependent amplitude coupling which includes diffraction losses. The frequency dependent amplitude coupling has been described in quantitative detail in reference [19]. The waveform and spectral amplitude curves are the average of six measurements. With this level of averaging the peak S/N for the waveform is approximately 200:1. The average transmitted power was 130 pW. The 170 meter path propagation at 50%

Received 4 Jan 2012; revised 20 Feb 2012; accepted 21 Feb 2012; published 8 Mar 2012

RH limits the transmission of frequency components to a maximum of about 0.95 THz. In addition, very weak water vapor transitions now appear in the spectrum at 0.184 THz, 0.326 THz, 0.474 THz, 0.659 THz, and 0.861 THz. Despite the strong effect of water vapor absorption there remain several regions of relative transparency which can be used for vapor sensing.

For the 170 meter path propagation we have also observed absorption features from the magnetic transitions of O_2. At ground level the amplitude absorption for the O_2 lines near 424.8 GHz and 834.1 GHz is predicted to be a few percent for a 170 meter path, which is approximately at the current detection threshold of our system (see below). While not shown here, we have found that these relatively weak absorption lines are more clearly observed under relatively dry conditions (RH < 10%).

3.2 Measurement of analyte vapors in the long-tube apparatus

The first example of a long-tube vapor measurement is for acetonitrile (CH_3CN) vapor. CH_3CN is a symmetric top molecule and its rotational spectroscopy has been well studied using high resolution methods [22,23]. For the case of atmospheric pressure broadening the rotational constant B is approximated as 9.199 GHz, which leads to a manifold of equally spaced rotational transitions separated by twice the rotational constant, 18.40 GHz. This separation is sufficient to allow resolution of the $J \rightarrow J + 1$ rotational bands under ambient pressure.

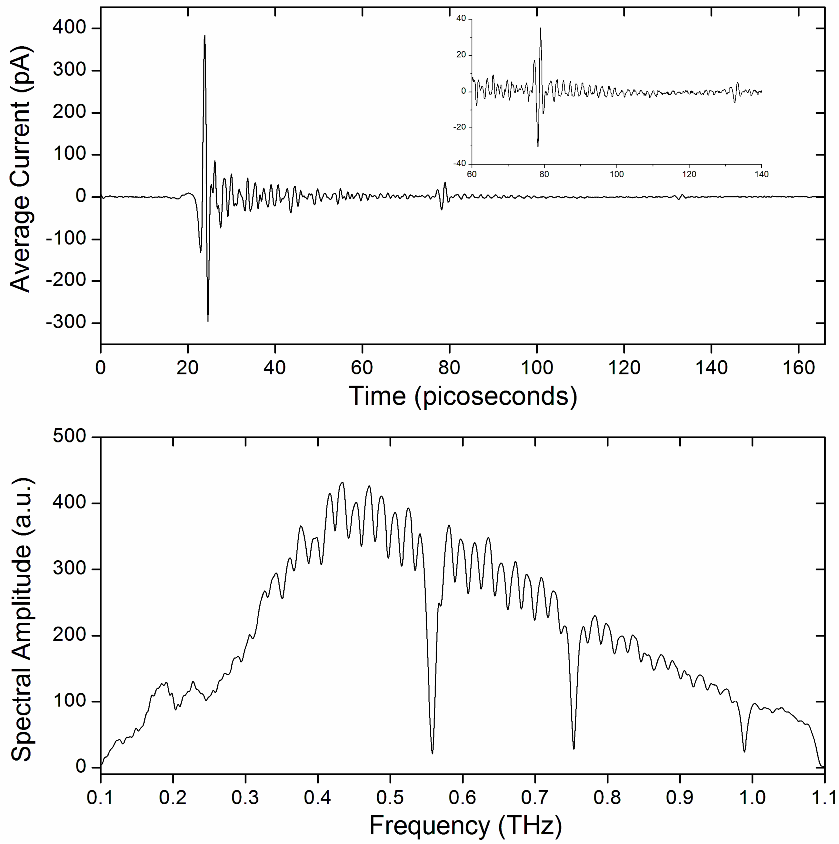

Fig. 5. Signal waveform (top) and spectral amplitude (bottom) for CH_3CN contained in the long-tube chamber at a concentration of approximately 200 ppm. The RH in the chamber was 14%. The inset shows the time base expanded in the echo region. The saturated absorption dips in the spectral amplitude are due to the strong water vapor rotational transitions.

Figure 5 (top) shows the signal waveform (average of four measurements) where the long-tube sample chamber contains CH_3CN at a concentration of approximately 200 parts per million (ppm). The RH in the sample tube was 14%. The waveform contains two components. The highly oscillatory pattern with large amplitude at early times is due to the interaction with the rotational transitions of water vapor. This signal decays sufficiently to expose a second component which consists of echo-like pulses centered near 79 ps and 133 ps. The echo pulses are a consequence of the coherent excitation of (nearly) equally spaced rotational transitions of the symmetric top molecule. Such echoes in THz transients were first observed by Harde et al. [24] and subsequently by Mittleman et al. [25], both using THz beams contained in a standard THz-TDS spectrometer, and without interference from water vapor. The observed recurrence time, τ, is approximately 54 ps, which corresponds to the inverse of

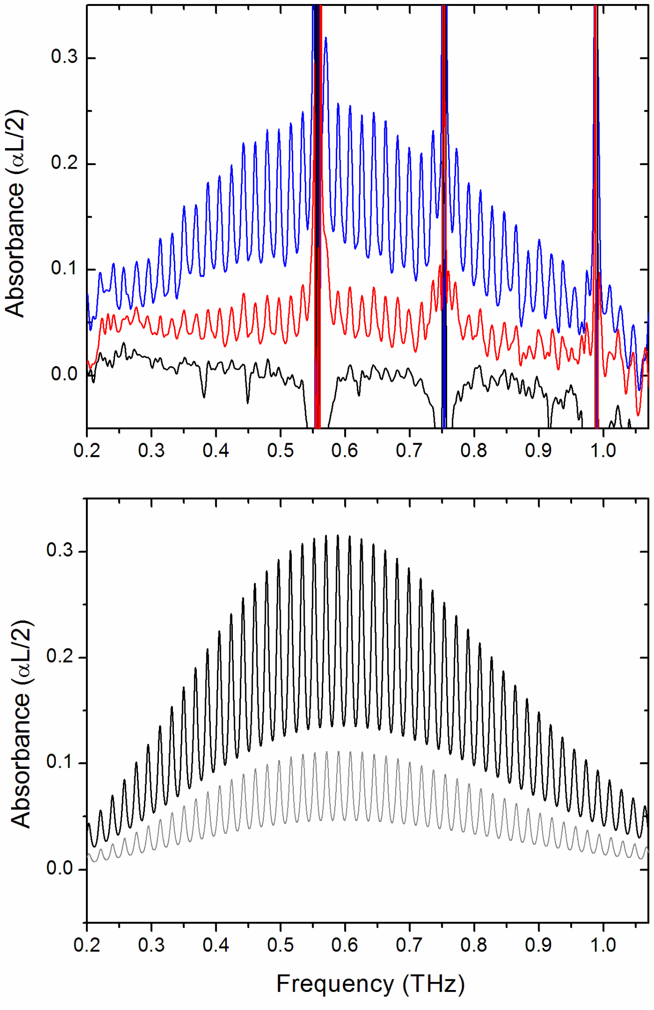

Fig. 6. (Top)Amplitude absorbance spectra for CH_3CN vapor contained in the long -tube at three concentrations: 200 ppm (top blue curve), 50 ppm (middle red curve), and 12 ppm (bottom black curve). Each curve represents the average of four measurements. The relative humidity for each measurement was 51%. (Bottom) Calculated absorbance spectrum for CH_3CN as described in the text. The solid black curve is the sum of the contributions from CH_3CN in the ground vibrational state and excited vibrational state v8 = 1. The solid gray curve is the calculated spectrum from CH_3CN(v8 = 1).

Received 4 Jan 2012; revised 20 Feb 2012; accepted 21 Feb 2012; published 8 Mar 2012

the frequency spacing ($\Delta\tau$ = 1/18.40 GHz)) between rotational bands. The decay of the echo pulses is to first order related to the collision broadened linewidth. We note that for the 6.7 meter path the echo pulses are easily observable at the low RH of 14% in the sample tube. At significantly higher RH the interference from the stronger water vapor signal would tend to obscure the echo pulses. Figure 5 (bottom) shows the Fourier transform of the waveform. Here, the spectral amplitude clearly shows the equally spaced rotational absorption bands. Superimposed on the spectrum is the nearly complete absorption due to the strong water vapor transitions at 0.55 THz, 0.75 THz, and 0.98 THz.

Figure 6 (Top) shows amplitude absorbance spectra for CH_3CN vapor at three concentrations inside the sample tube: 200 ppm, 50 ppm and 12 ppm [20]. The amplitude absorbance is the natural logarithm ($\alpha L/2$) of the ratio of the signal amplitude spectrum to the reference amplitude spectrum. These measurements were made at a much higher RH of 51%. The strong modulations in the spectrum are due to the incomplete removal of saturated water vapor absorption. At the highest concentration the rotational manifold of CH_3CN is clearly observed. The $J \rightarrow J + 1$ bands are not fully resolved because of the combined pressure and instrument broadening. We also note that each absorption band contains a superposition of non-degenerate $K \rightarrow K$ transitions, which add slightly to the width of the absorption bands. In the region where S/N is the highest (0.4 – 0.7 THz) the frequencies can be measured with a precision of about ± 0.5 GHz.

In addition, CH_3CN has a relatively low frequency vibrational mode (v8) at 365.05 cm^{-1}, which is doubly degenerate (v8 = 1, $B \approx 9.226$ GHz [23]; v8 = 2, $B \approx 9.252$ GHz [23]). At room temperature the THz absorption from vibrationally excited CH_3CN is non-negligible. The rotational bands of CH_3CN (v8) will have a frequency-dependent offset from ground state CH_3CN because of the different rotational constant in the excited vibrational state.

As the CH_3CN vapor concentration is lowered to 50 ppm the amplitude absorbance becomes correspondingly smaller. The limit of our detection sensitivity occurs near a concentration of approximately 12 ppm, where an experimental amplitude absorbance of about 1% is measured with S/N~1. The negative amplitude absorbance near the water vapor lines resulted from a slight decrease in the humidity level in the sample tube during the data collection for the 12 ppm sample.

We compare the experimental spectrum for CH_3CN to the theoretically predicted spectrum using database values for the CH_3CN line frequencies and line intensities that are tabulated in the JPL spectral line catalog [26]. The absorption coefficient between pairs of *J,K* levels in CH_3CN can be calculated using

$$\alpha_{J,K}^{\mathrm{v}}(\nu) = S_{J,K}^{\mathrm{v}} \cdot g(\nu) \cdot N \cdot P_o, \tag{1}$$

where $a_{J,K}^{\mathrm{v}}(\nu)$ is in cm^{-1}, $S_{J,K}^{\mathrm{v}}$ is the line intensity (cm^{-1}/molecule cm^{-2}) for a $J \rightarrow J + 1$, $K \rightarrow K$ transition, the index v represents the vibrational state, N is the number density (molecules/(cm^3-atm)), P_o is the partial pressure of the analyte vapor (atm), and $g(v)$ is the Lorentz lineshape function,

$$g(\nu) = \frac{1}{\pi}\left[\frac{\Delta\nu}{(\nu_{J,K} - \nu)^2 + \Delta\nu^2}\right], \tag{2}$$

with transition frequency $v_{J,K}$, and, for simplicity, the half width Δv is taken to be the sum of the pressure broadening and a Lorentzian-type instrumental width, $\Delta v_p + \Delta v_{instr}$. The spectrum is obtained by summing over *J,K* states and vibrational states v. For our calculation we only consider the ground vibrational state v = 0 and the low frequency mode v8 = 1, for which the values of transition frequency and line intensity are available in the JPL catalog,

$$\alpha(\nu) \approx \sum_{J,K} [\alpha_{J,K}^{\mathrm{v}=0}(\nu) + \alpha_{J,K}^{\mathrm{v8}=1}(\nu)]. \tag{3}$$

#160928 - $15.00 USD Received 4 Jan 2012; revised 20 Feb 2012; accepted 21 Feb 2012; published 8 Mar 2012

For most molecules in the JPL catalog only the rotation-spin partition function is considered in the calculation of the line intensities. However, in the case of CH_3CN in the ground vibrational state the partition function incorporates vibrational states up to about 1200 cm^{-1} in the partition function [26]. Incorporation of the vibrational partition function for CH_3CN (v8 = 1) is not mentioned [26], therefore we scaled the $S_{J,K}^{v8=1}$ by the vibrational partition function using the harmonic oscillator approximation,

$$Z_{Vib} = \prod_i \left[1 - \exp(-\frac{E_{vib}}{kT}) \right]^{-d_i}, \tag{4}$$

where the product runs over the vibrational modes, and d_i is the degeneracy. Only the lowest vibrational mode v8 is considered leading to $Z_{Vib} \approx 1.46$. The $S_{J,K}^{v}$ are converted from JPL units of nm^2-MHz to units of cm^{-1}/(molecule cm^{-2}), and then multiplied by the fractional abundance I_a of the main isotopologue [27],

$$S_{J,K}^{v}(cm^{-1} / molecule \times cm^{-2}) = \frac{I_a S_{J,K}^{v}(nm^2 MHz)}{2.99792458 \times 10^{18}}. \tag{5}$$

We have not scaled the $S_{J,K}^{v}$ from their tabulated values at 300 K to the experiment at 298 K. This represents a small correction for the current experimental sensitivity. In the calculation $\Delta v = 5$ GHz, $N = 2.46 \times 10^{19}$ molecules/(cm^3-atm), $P_o = 2 \times 10^{-4}$ atm, and $L = 540$ cm. Figure 6 (bottom) shows the calculated amplitude absorbance for CH_3CN from Eq. (3), and the contribution made by CH_3CN(v8 = 1). The frequency-dependent offset of the CH_3CN (v8 = 1) rotational bands slightly broaden the rotational bands in the summed spectrum and to add to the absorption pedestal. The calculated peak amplitude absorbance of about 0.31 is in approximate agreement with the peak experimental absorbance of 0.25. We note, however, that the calculated absorbance does not contain contributions from CH_3CN (v8 = 2). A comparison of the peak band frequencies of experimental and calculated spectra shows agreement to within 1 GHz.

In the second example described below in Fig. 7, drops of liquid D_2O were introduced into the sample tube containing laboratory air at RH = 51%. The evaporation of the drops was facilitated by slightly heating the tube from underneath. Assuming complete vaporization, the volume of liquid corresponds to a vapor concentration of approximately 750 ppm in the sample tube volume. Figure 7 (top) shows the reference spectral amplitude (top black curve, no D_2O present) and the signal spectral amplitude (bottom red curve, with D_2O present). There are twelve absorption dips in the region between 0.4 – 1.0 THz due to the analyte vapor. Eight of these are indicated by the blue arrows. The inset to Fig. 7 (top) shows the frequency region between 1.2 – 1.6 THz, where the spectral amplitude returned to the receiver is relatively small, but still sufficient to observe an additional eight absorption lines.

Figure 7 (bottom) shows the absorbance spectrum between 0.4 – 0.95 THz (black line) derived from the signal and reference spectral amplitudes. As before, the saturated absorption due to the strong water vapor lines cannot be removed. Even so, up to 12 absorption lines due to the analyte can be observed in this region. However, upon comparison with the JPL catalog [26], we find that the majority of the line frequencies agree with the rotational transitions of semi-heavy water vapor, HDO. In the presence of H_2O the H and D atoms will rapidly exchange according to the reaction: $H_2O + D_2O \leftrightarrow 2HDO$. In the presence of excess H_2O the equilibrium will be driven to increase the concentration of HDO. The conversion to HDO is likely facilitated by interaction with H_2O on the walls of the tube. To determine the extent of the conversion we fit the experimental absorbance spectrum to a superposition of D_2O and HDO absorbance spectra using the line frequencies and line intensities from the JPL catalog [26] (which are then converted using Eq. (5)) and varied the ratio of HDO:D_2O spectra to obtain a best fit. A 3.5 GHz HWHM linewidth is used. The best fit is shown as the red curve in Fig. 7 and corresponds to a ratio of 22:1 HDO:D_2O. An isolated D_2O absorption near 0.693

Received 4 Jan 2012; revised 20 Feb 2012; accepted 21 Feb 2012; published 8 Mar 2012

THz is indicated by the black arrow in Fig. 7. The fit implies that about 92% of D_2O has converted to HDO. The closeness of the fit to the experimental spectrum indicates the stability of the THz-TDS long-tube apparatus and confirms the ability to determine the line frequencies with accuracy better than 1 GHz in the spectral range shown. Similar to the case of CH_3CN shown above, an amplitude absorption of about 1% can be resolved with S/N ~1 with an average of four measurements.

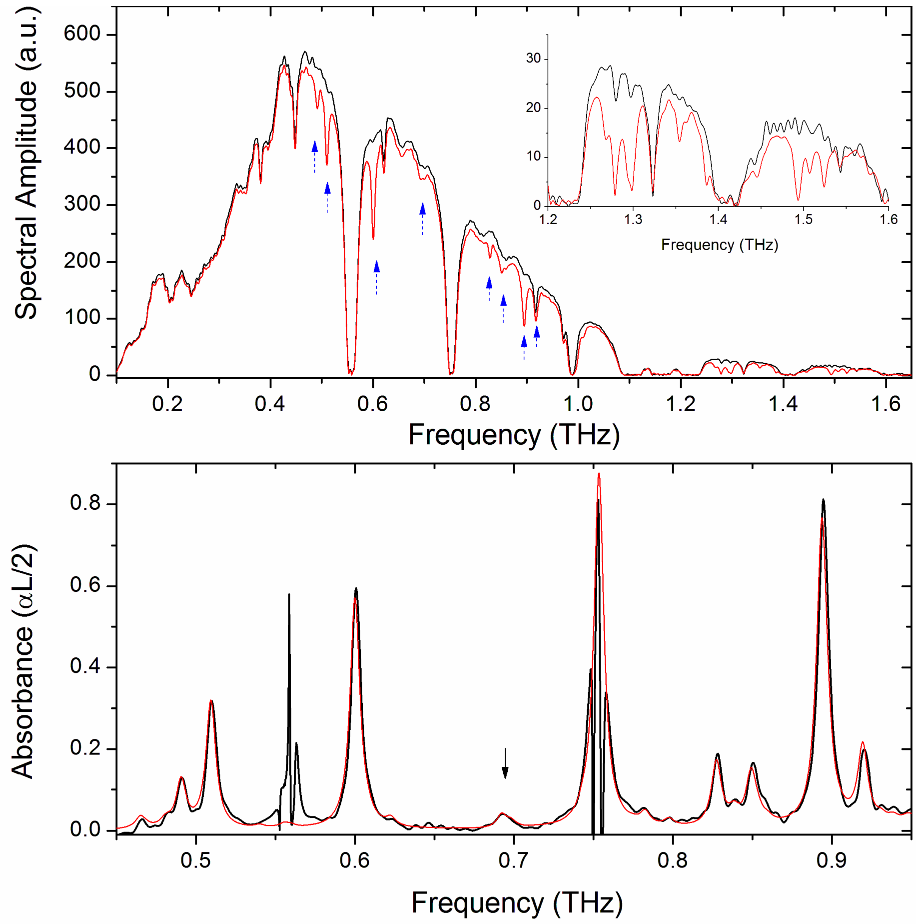

Fig. 7. Top panel: Spectral amplitudes for the reference (top black curve) and signal (red curve) where D_2O liquid drops are introduced to the sample tube corresponding to a vapor concentration of 750 ppm and at RH = 51%. The blue arrows indicate absorption resonances due to analyte vapor. The areas of complete absorption are due to strong water vapor lines. The inset shows absorption resonances in the expanded higher frequency range. Bottom panel: Amplitude absorbance spectrum derived from the curves of the top panel. The black curve is the experimental absorbance. The strong modulations near 0.55 THz and 0.75 THz are due to the saturated absorption from water vapor. The red curve is a fit to the experimental absorbance using line frequencies and line strengths for HDO and D_2O contained in the JPL catalog. The black arrow indicates an isolated absorption due to D_2O.

3.3 Measurements of analyte vapors in the long-path apparatus

The measurement of target vapors over the much longer 170 meter round trip path is more challenging because of increased water vapor absorption, greater fluctuations in humidity, and thermal and mechanical fluctuations leading to variations THz pulse path length. The strong effect of water vapor absorption on the THz waveform from the 170 meter path propagation was shown in Fig. 4. In this section we investigate the ability of the long-path apparatus outlined in Fig. 3 to measure the rotational spectra of CH_3CN and the HDO/D_2O mixture. Figure 8 compares spectral amplitudes for the reference (upper black curve) where the sample chamber (1.2 meter round trip path length) contains ambient air only and signal (lower red curve) where the sample chamber contains CH_3CN vapor at a concentration of 800 ppm mixed with ambient air. The higher concentration is used to achieve similar absorption strength as for the 4.5 times longer PVC tube. Each of the curves is the average of six separate measurements. The laboratory RH was 50%. Within the transmission windows several of the rotational absorption bands are clearly observed as dips in the spectral amplitude signal.

In the measurement, six reference waveform scans were collected first (no CH_3CN in the chamber) and the spectral amplitudes averaged to obtain the reference spectrum. CH_3CH was then introduced to the chamber and allowed to equilibrate, and six signal waveforms collected and the spectral amplitudes averaged to obtain the signal spectrum. As a check of the system and environmental stability, a second set of six reference scans were taken. Typically we found that the two sets of reference spectra showed agreement to within 5%. A full sequence of measurements required about 1 hour to complete.

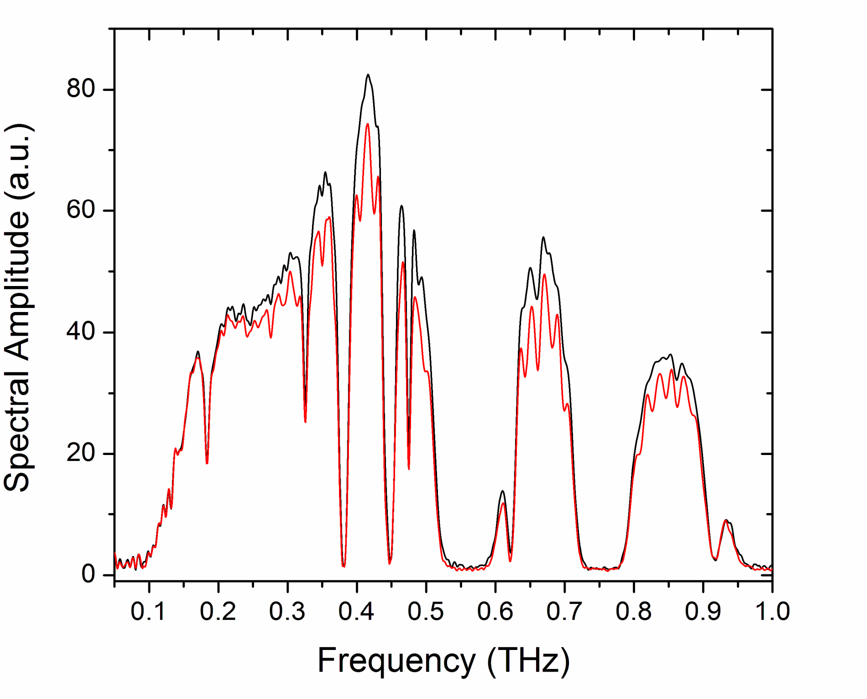

Fig. 8. Spectral amplitudes for the reference (upper black curve) and the sample chamber containing CH_3CN (lower red curve) for the 170 meter path measurement. The concentration of acetonitrile is 800 ppm in the sample tube. The laboratory relative humidity was 50%.

The corresponding absorbance spectrum is shown below in Fig. 9 (top). The hatched areas indicate regions of complete absorption by water vapor, consequently rotational transitions of the analyte cannot be observed in these regions. However, in the transmission windows as many as 20 rotational bands can be observed. From Fig. 4 the peak of the spectral amplitude is approximately 3-4 times smaller than for the long-tube measurements, which leads to a correspondingly smaller signal to noise ratio. A measure of the minimum detectable absorption is given in Fig. 9 (bottom) showing the noise baseline recovered from averaging six pairs of reference measurements. Depending on the position within the transmission windows the minimum detectable amplitude absorption (S/N ~1) varies between 2.5 – 5%.

Received 4 Jan 2012; revised 20 Feb 2012; accepted 21 Feb 2012; published 8 Mar 2012

This may be compared to the minimum detectable amplitude absorption of ~1% obtained with the long-tube apparatus.

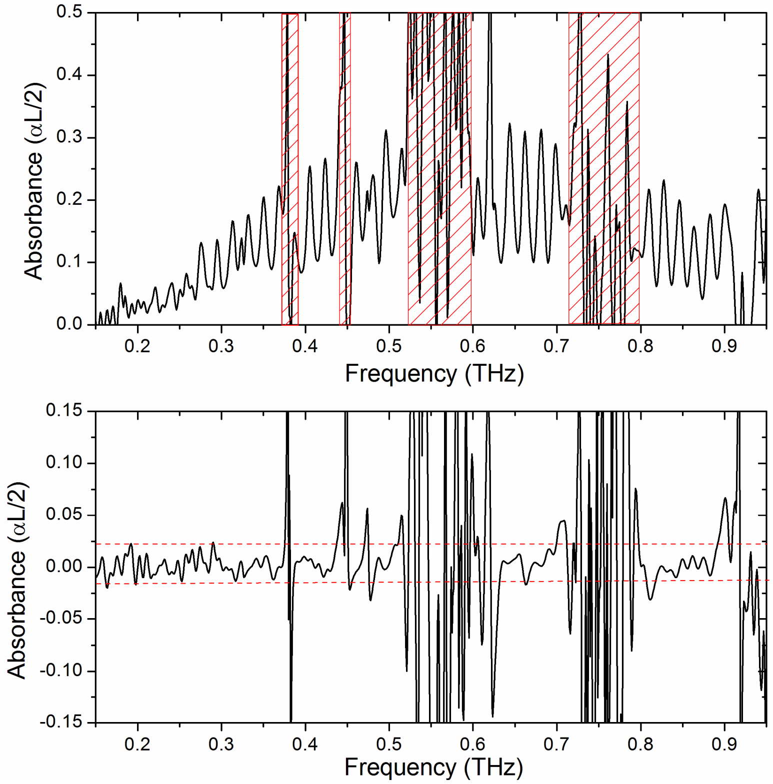

Fig. 9. (Top) Amplitude absorbance spectrum for CH_3CN vapor at 800 ppm in the 1.2 m (round-trip) sample chamber measured using the 170 meter long-path apparatus. The laboratory relative humidity was 50%. The hatched areas indicate regions of complete water vapor absorption. The curve is the average of six signal and reference measurements (Bottom) Noise baseline from the average of six pairs of reference measurements. The red horizontal bars provide a qualitative measure of the noise level in the amplitude absorbance.

The final example shown below in Fig. 10 is the detection of a HDO/D_2O vapor mixture contained in the sample chamber within the 170 meter THz path. Here, D_2O liquid is initially evaporated in the sample chamber in an amount equivalent to a vapor concentration of approximately 3000 ppm. As before, the four-fold larger concentration (compared to the long-tube measurement) is used to compensate for the shorter interaction path. Figure 10 (black curve) shows the experimental amplitude absorbance for the HDO/D_2O mixture in the presence of 50% RH. The result is the average of eight measurements. Despite the much increased effect of water vapor absorption and lower S/N compared to the corresponding long-tube measurement, seven absorption lines marked by blue arrows can be distinguished from the noise floor and are due to the analyte vapors. The red curve is the fit to the experimental spectrum based on a superposition of HDO and D_2O database line frequencies and relative line intensities. The best fit occurs for a 2.4:1 ratio of $HDO{:}D_2O$. Compared to the long-tube case, a smaller percentage of the initial D_2O introduced to the chamber has converted to HDO. Also from the fit we find that the accuracy of the experimental line frequencies is within 1.5 GHz of the JPL catalog values. This finding is an indication the stability of the long-path apparatus over the approximate 1 hour time to perform the reference measurements, introduce and equilibrate the sample, and the perform the signal measurements.

Received 4 Jan 2012; revised 20 Feb 2012; accepted 21 Feb 2012; published 8 Mar 2012

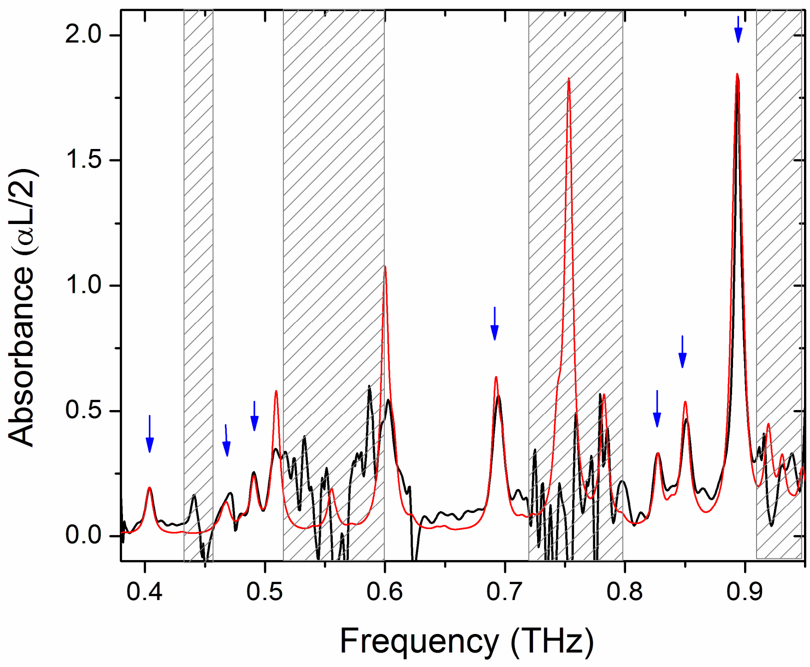

Fig. 10. Experimental amplitude absorbance spectrum (black curve) where D_2O liquid is introduced into the 1.2 m (round-trip) sample chamber to give a concentration of approximately 3000 ppm. The relative humidity in the laboratory and sample chamber is 50%. The hatched areas indicate regions of complete absorption by water vapor. The red curve is a fit to the experimental spectrum using rotational line frequencies and line intensities for HDO and D_2O contained in the JPL catalog. The fit indicates a relative fraction of HDO:D_2O of 2.4:1.

It's useful to discuss the sensitivity of the long-path system to the detection of various small molecule gas/vapor analytes. With respect to Eq. (1), we use the molecular cross section $\sigma_{i,j} = S_{j,k} g$ (cm^2/molecule) for a transition between states *i* and *j*, and the column density, $u = NP_o L$ (molecules/cm^2). From this we estimate the column density needed to detect an analyte using the ~3% criterion for amplitude absorption (~6% power absorption). For CH_3CN in the ground vibrational state we consider the rotational band corresponding to the $J = 36 \rightarrow 37$ transition in the transmission window near 0.680 THz. A HWHM width of 3.5 GHz for the combined pressure broadening and instrumental broadening is used for the lineshape factor, *g*. Summing over the $K \rightarrow K$ transitions contained in the JPL database yields an absorption cross section of approximately 2.4×10^{-19} cm^2/molecule (scaled for the fractional abundance of CH_3CN), which yields a column density of 2.5×10^{17} molecules/cm^2 (equivalent to 100 ppm-m) needed for a 3% amplitude absorption. This may be compared to cases of a relatively strong absorbing gas, such as HCN, and a relatively weak absorbing gas, such as H_2S. For these molecules we use values from the JPL database scaled for the main isotopologue. The vibrational partition function is not considered here. For isolated rotational lines in transparency windows we find for HCN with $\nu \approx 0.886$ THz and $\Delta\nu = 3.5$ GHz: $\sigma \approx 1.7 \times 10^{-18}$ cm^2/molecule; and for H_2S with $\nu \approx 0.708$ THz and $\Delta\nu = 3.5$ GHz: $\sigma \approx 1.3 \times 10^{-20}$ cm^2/molecule. For a 3% amplitude absorption the column densities are approximately 3.7×10^{16} molecules/cm^2 (15 ppm-m) for HCN and 4.8×10^{18} molecules/cm^2 (1900 ppm-m) for H_2S. For our current system with 120 ms acquisition time per waveform time step and three minutes per 625 point waveform scan, then the collection of eight signal and eight reference

Received 4 Jan 2012; revised 20 Feb 2012; accepted 21 Feb 2012; published 8 Mar 2012

scans for 3% sensitivity requires a minimum of 48 minutes. As mentioned above, an optimized data acquisition system might approach 75 seconds per scan, or 20 minutes for the set of eight signal and eight reference scans.

4. Summary and outlook

Using a modified THz-TDS spectrometer we have demonstrated detection of rotational spectra of analyte vapors located remotely from the spectrometer and under ambient laboratory conditions of temperature, pressure, and humidity. Two types of apparatus were investigated. First, in the long-tube configuration the detection of the signature echo pulses from CH_3CN was demonstrated in the presence of low relative humidity of 14%. The interference of the water vapor signatures obscures the echo transient at the higher relative humidity of 51%. However, here, we were able to detect the absorbance spectra of analyte vapors over a broad range of frequencies from 0.2 - 1.6 THz. The minimum detectable amplitude absorption was shown to be approximately 1%. Second, we demonstrated detection of rotational transitions when the THz beam propagated over a much longer 170 meter open path in the ambient laboratory environment, subject to increased losses due to water vapor absorption, amplitude coupling and diffraction, as well as increased environmental fluctuation in humidity, temperature, and mechanical vibration. In this more challenging environment we showed that the long-path apparatus had sufficient stability to detect rotational line amplitude absorption as small as about 3-5%. The increased THz loss due to water vapor absorption limited detection to the transparency windows below about 1 THz. To our knowledge, both of these demonstrations represent the first of their kind for broadband ultrashort THz pulses.

To assess the potential of using broadband THz pulses for remote sensing applications it's important to discuss current limitations in detection sensitivity, as well as the type of vapors where this method can achieve specificity. Our current THz-TDS system uses only about 10 mW of optical power to gate each the transmitter and receiver, out of more than 300 mW that is available. The 10 mW optical beam generates a low power beam of THz pulses with about 30 nW of average power. After propagation of 170 meters, with losses due to water vapor absorption, coupling back to the receiver, and diffraction, it was determined in Ref [18]. that the returned power was reduced to 130 pW. Even so, the THz waveform can be measured with S/N of 200 (baseline to peak). There is potential to significantly increase S/N through a combination of increasing the generated THz power, optimizing the THz pulse spectrum for overlap with the atmospheric transparency windows, and reducing diffraction loss. For example, by using larger feature size photoconductive antennas, or interdigitated antennas [28], it should be possible to gate the transmitter and receiver with 100 mW of optical power. In principle, this modification alone could lead to a 100-fold increase in the detected THz signal power. Higher THz power levels would be useful to reduce the signal acquisition time for detection.

Pressure broadening places a limitation on the generality of THz sensing of vapors in the ambient environment. The relatively light molecules discussed here represent favorable cases because of the small partition functions and large separation between rotational lines. Qualitatively, for molecules that can be described as symmetric tops, a 5 GHz FWHM pressure-broadened line width implies that the rotational constant (total angular momentum) should not be much smaller than 5 GHz in order to at least partially resolve the rotational bands. Therefore, at atmospheric pressure, specificity is maintained only for the class of relatively small and light vapor molecules with relatively large rotational constants. However, it should be mentioned that the detection of small molecules such as HCN, HCl, H_2S, and CH_2CO, are relevant to the sensing of toxic gases and vapors. Heavier molecules are far more challenging for detection because of their large partition functions and more complex spectra, which tend to merge into broad absorption features at ambient pressure, compromising specificity. We note that to increase specificity and extend the generality of THz sensing to larger molecules an infrared-THz double resonance method has been recently proposed [29].

Sensing in the field will be more challenging because of atmospheric fluctuations in humidity, temperature, pressure, and increased mechanical vibrations. These atmospheric fluctuations can affect the repeatability of signal and reference measurements conducted over a given time duration. There is also uncertainty in projected detection levels of analytes due to uncertainties in the level of moist and dry air continuum absorption which are pressure and temperature dependent, and due to line mixing [30] (collision-induced coupling of energy levels undergoing a transition) which can be significant at ambient pressure. The extent to which the atmospheric fluctuations mentioned above affect detection using THz-TDS remains to be determined.

Appendix Comparison of THz-TDS with far-infrared FTS

With respect to recent and ongoing experimental work cited in the introduction, that uses far-infrared FTS to study the atmosphere and the continuum absorption of water vapor, the following comparison between THz-TDS and FTS is provided. For THz-TDS the detection of THz (far-infrared) radiation is extremely sensitive. Although the energy per THz pulse is usually very low (0.3 femtoJoule), the 100 MHz repetition rate and the coherent detection measures the electric field of the propagated pulse with a signal-to-noise ratio of up to 10,000 with an integration time of 125 msec [31], for the incoming beam with an average power of 30 nW. In terms of the average power, this room-temperature sensitivity exceeds that of the liquid helium cooled bolometers used in FTS by more than 1000 times [32]. Because of the gated and coherent detection, the thermal background, which plagues FTS measurements in the far-infrared, is observationally absent. The THz beams are spatially coherent and well collimated, allowing for excellent shielding from scattered radiation and for tight coupling to the receiver with an extremely small solid angle of detection to further discriminate against scattered and thermal radiation.

The opto-electronically excited, subwavelength Hertzian dipole antenna of the THz transmitter can be considered as a point source for the analysis of the diffraction effects of the entire THz optical train. For our long-path system, the returning beam of the THz pulses captured by our 30 cm diam. telescope mirror is focused to the diffraction limited spot size of Si lens optically coupled to Hertzian dipole antenna of the receiver. This spot size diameter is approximately the free-space wavelength divided by the THz index of refraction of Si, n = 3.42. This diffraction limited focusing is in contrast to that for the FTS extended source of an arc lamp or hot glow bar.

The frequency resolution of the two techniques are similar, since they are both based on a scanning delay line, where to first order the frequency resolution is determined by the reciprocal of the time scan. As demonstrated in references. 9 and 10, long scan FTS can achieve at least ~ 200 MHz spectra resolution. In principle, similar resolution can be achieved using opto-electronic THz-TDS methods. However, in practice, the scan length in THz-TDS is often limited to smaller lengths by reflections in the THz pulse train that occur within the optically gated antennas. These reflections can be difficult to eliminate.

A powerful advantage of THz-TDS is that the electric field pulse is measured. In the 10 nsec time interval between the sub-picosecond THz pulses there is essentially no power from the THz transmitter, only incoherent noise. This situation plus the fact that the THz receiver is gated to eliminate the incoherent thermal radiation between pulses, allows for the extremely high S/N values for the measured electric field pulses. A subsequent numerical Fourier transform of the measured THz sample pulse gives the complex amplitude spectrum, a product of the amplitude spectral response of the receiver, the sample and transmitter. Dividing this complex spectrum by that of the THz reference pulse (measured THz pulse with no sample in place), gives the complex amplitude spectral response of the sample [33].

In contrast, FTS typically measures (with helium cooled bolometers) the transmitted THz (far-infrared) power from an interferometer as a function of the relative path difference between the two arms [34]. Assuming an incoherent source, the resulting interferogram has the form

$$I(\Delta)=\sum_{\omega}\left[E_1(\omega)^2+E_2(\omega)^2+2E_1(\omega)E_2(\omega)\cos(k_{\omega}\Delta)\right],$$

where $E_1(\omega)$ and $E_2(\omega)$ are the field amplitudes in arms 1 and 2 for frequency ω; $\Delta = l_1 - l_2$ with l_1 and l_2 the length of arms 1 and 2; k_ω is the propagation vector for frequency ω. For the usual case of $E_1 = E_2$, the magnitude of the interference peak at zero relative delay is equal to the constant background power. Fluctuations in this background are a major source of noise in the measurement. A numerical Fourier transform of the FTS interferogram gives the power spectrum. The d.c. component from the constant background power is neglected. Dividing the power spectrum of the sample FTS interferogram, obtained by placing a sample between the interferometer and the bolometer, by that of the reference FTS interferogram (no sample in place) gives the power transmission of the sample.

The THz pulse measurement and the FTS interferogram are comparable objects. Both allow for spectroscopic determinations, using the sample-in, sample-out sequence to generate the two corresponding THz pulse measurements, or FTS interferograms. For similar S/N ratios of the THz pulse and the FTS interferograms, extending over the same scan length of their respective delay lines, the S/N ratio of the THz pulse amplitude spectrum and the FTS power spectrum would be comparable.

An excellent S/N ratio for the THz pulse is 10,000, while for the FTS interferogram in the same far-infrared spectral range an excellent S/N ratio is 2000 [34]. Thus, THz-TDS has a potential 5X, S/N advantage over FTS in the frequency range from 0.2 up to about 4 THz. In addition, the IFFT of the THz pulse measurements provide the complete complex amplitude spectral response of the sample, compared to the power spectral response provided by the power interferogram. Comparing the power spectrum of FTS with the power spectrum for THz-TDS, which is the square of the amplitude spectrum, and for which the power S/N is equal to the amplitude (S/N) squared, illustrates the potential for THz-TDS to make entirely new type measurements. Such an example is the THz-TDS characterization of flames [21].

Acknowledgments

This work was supported by the Defense Threat Reduction Agency (11-2210M), the Office of Naval Research, and the National Science Foundation.